JPE 17-3-22

https://doi.org/10.6113/JPE.2017.17.3.798
ISSN(Print): 1598-2092 / ISSN(Online): 2093-4718

A Hybrid Static Compensator for Dynamic Reactive Power Compensation and Harmonic Suppression

Jia-qiang Yang†, Lei Yang*, and Zi-peng Su*

†,*College of Electrical Engineering, Zhejiang University, Hangzhou, China

Abstract

This paper presents a combined system of a small-capacity inverter and multigroup delta-connected thyristor switched capacitors (TSCs). The system is referred to as a hybrid static compensator (HSC) and has the functions of dynamic reactive power compensation and harmonic suppression. In the proposed topology, the load reactive power is mainly compensated by the TSCs. Meanwhile the inverter is meant to cooperate with TSCs to achieve continuous reactive power compensation, and to filter the harmonics generated by nonlinear loads and the TSCs. First, the structure and mathematical model of the HSC are discussed Then the control method of the HSC is presented. An improved reduced order generalized integrator (ROGI)-based selective current control method is adopted in the inverter to achieve high-performance reactive and harmonic current compensation. Meanwhile, a switch control strategy is proposed to implement precise and fast switching of the TSCs and to avoid changing the time delay needed by the conventional switch strategy. Experiments are implemented on a 20 KVA HSC prototype and the obtained results verify the validity of the proposed HSC system.

Key words: Harmonic suppression, Hybrid static compensator (HSC), Reactive power compensation, Reduced order generalized integrator (ROGI), Switch control strategy

I. INTRODUCTION

A lot of power electronic devices and nonlinear loads have been widely used in power systems, which results in a lot of serious problems, including reactive power and harmonic pollution. The presence of reactive power and harmonics is detrimental to the grid, because it causes additional power losses and malfunctions of the grid components. Thus, reactive power compensation and harmonic suppression have become popular issues in recent research [1]-[3].

Thyristor switched capacitors (TSCs) are the most commonly used device for reactive power compensation. They have the characteristics of a simple structure, low loss and low maintenance requirements. The reactive power output of a TSC can be changed step by step through switching the thyristor on or off. Several TSCs can be combined for large-capacity reactive power compensation at a low cost. However, TSCs have a relatively slow response time, and they cannot implement continuous reactive power compensation [4], [5]. Static Var Compensators (SVCs) are also useful. However, they introduce harmonic currents into the grid [6]-[8]. Active power filters (APFs) have been developed for harmonic suppression and reactive power compensation since the 1970s [9]-[11]. These devices have good performances, such as high steady-state compensation precision, fast dynamic response, low probability of resonance with the grid, etc. However, the cost of an APF is relatively high so that it is unsuitable for a large-scale systems [12]-[14]. The aforementioned devices can individually improve the power quality of the grid. However, they also have limitations. Thus, many hybrid systems have been proposed to achieve superior performance [15]-[17].

In low-voltage distribution grids, a kind of electronic device with harmonic suppression and large-capacity reactive power compensation is widely needed. In [16], the authors presented a dynamic hybrid var compensator (HVC) that is composed of a small-rate distribution static compensator (DSTATCOM) and multigroup TSCs. The HVC can implement large-capacity continuous reactive power compensation. However, multiple current sensors are necessary for simultaneously detecting the TSC current and the load current, which increases the system complexity. In [17], a combined system of an APF, a thyristor controlled

Manuscript received Oct. 12, 2016; accepted Feb. 17, 2017
Recommended for publication by Associate Editor Kyo-Beum Lee.
†Corresponding Author: yjq1998@163.com
Tel: +86-571-8795-1784, Fax: +86-571-8795-1625, Zhejiang Univ.
*College of Electrical Engineering, Zhejiang University, China

reactor (TCR) and a fixed capacitor (FC) was proposed. The system has the functions of power factor correction and harmonic suppression. However, it is difficult to dynamically adjust the high capacity reactive power due to the FC.

In this paper, a HSC system is proposed for dynamic reactive power compensation and harmonics suppression. The HSC is a typical hybrid system that is composed of a small-capacity inverter and multigroup delta-connected TSCs. Both the control of the inverter and the TSCs can influence the system performance. The inverter is meant to cooperate with the TSCs to achieve smooth reactive power compensation and to filter harmonic currents. The current control method adopted in the inverter directly determines the performance of the current compensation. However, some common control methods, such as PI control [18], fuzzy control [19], sliding-mode control [20] and adaptive control [21], can attenuate current harmonics only to a certain level, and cannot realize high current compensation precision. Consequently, a high-performance current control method is required for controlling the inverter. On the other hand, TSCs are used to compensate the major reactive power of the load, and their reactive power output can be changed step by step. Therefore, a fast and precise switch control strategy is needed to control the switching of the TSCs. Traditionally, the power factor (PF) is chosen as a reference, and the TSCs are switched to satisfy the requirement of the PF. A fixed time delay is usually added to ensure that the switching of the TSCs is operated when the load reactive power is restored to the steady state. However, a suitable time delay is difficult to set because practical load changes are uncertain [22], [23].

Based on the proposed HSC system, a ROGI-based current control method is presented to realize high-performance reactive and harmonic current compensation. Meanwhile, a precise and fast switch control strategy is adopted without changing the time delay under different load changes. This paper is organized as follows. Section II introduces the structure and compensating principle of the HSC and gives the mathematical model. Section III analyzes the mathematical model of the inverter, and proposes a ROGI-based selective current compensation method. Section IV introduces the proposed switch control strategy. Section V presents experimental results, and Section VI draws some conclusions.

II. HSC Control System and Mathematical Model

A. HSC Structure and Compensating Principle

The structure of the proposed HSC is shown in Fig. 1. The HSC is composed of several thyristor switched capacitors (TSC) and a two-level voltage source inverter with a DC capacitor and an LCL-type output filter. A three-phase diode rectifier with a resistive and inductive load is adopted as a harmonic source to produce harmonic currents. In addition, a three-phase linear inductive load can be connected in parallel with the nonlinear load to produce the necessary reactive current.

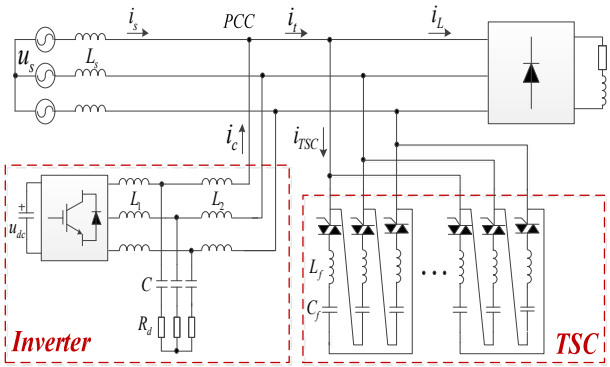

Fig. 1. Structure diagram of the HSC.

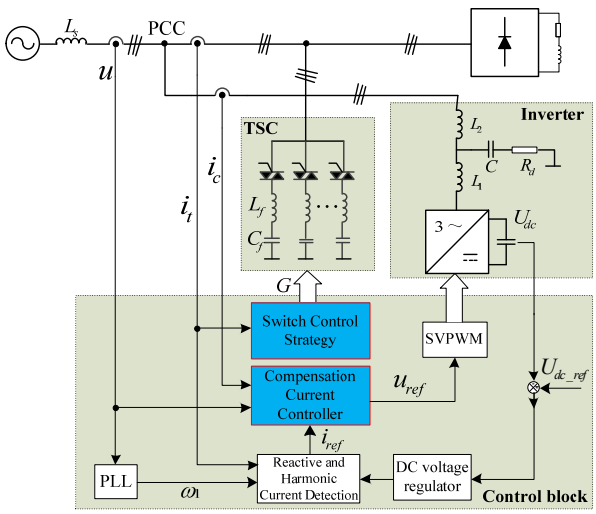

Fig. 2. Block diagram of the HSC control system.

In Fig. 1, u_s denotes the grid voltage, L_s denotes the grid impedance, and i_s denotes the grid current. i_l denotes the load current, i_{TSC} denotes the current of the TSCs, i_c denotes the output current of the inverter, and i_t denotes the current sum of i_l and i_{TSC}. PCC denotes the point of common coupling. In the inverter, L_1 denotes the inverter-side filter inductor, L_2 denotes the grid-side filter inductor, C denotes the filter capacitor, R_d denotes the damping resistor, and u_{dc} denotes the voltage of the DC capacitor. In each TSC, an inductor and a capacitor are in series and inverse parallel couple silicon-controlled rectifiers (SCR) are used as an electric switch. L_f and C_f denote the inductor and capacitor of the TSC, respectively.

A block diagram of the HSC control system is presented in Fig. 2. The control system contains a reactive and harmonic current detection link, a DC voltage regulator, a compensation current controller and a switch control strategy link. The reactive and harmonic current detection link detects the reactive and harmonic components in the total currents of

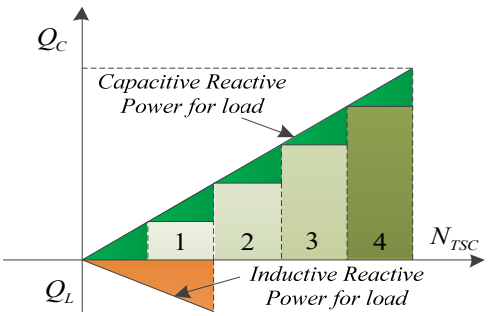

Fig. 3. Compensating principle of the HSC.

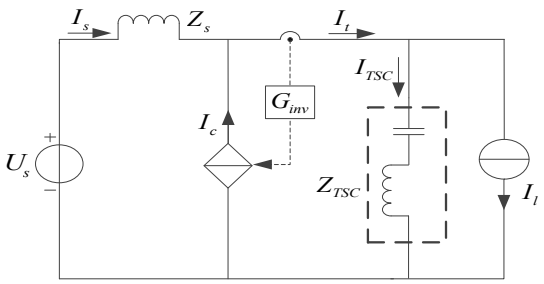

Fig. 4. Single-phase equivalent circuit of the HSC.

the load and TSCs. A DC voltage regulator is adopted to maintain the DC bus voltage stability. The compensation current controller generates a reference voltage that allows the compensation current to track the reference current accurately. The switch control strategy link generates the switching signal to operate the TSCs. Therefore, the total compensation current of the HSC can offset the reactive and harmonic components in the load currents, and the power quality in the PCC is also improved.

The compensating principle of the HSC is presented in Fig. 3. N_{TSC} is the number of TSCs which are switched onto the grid, and Q_C and Q_L are the output capacitive reactive power and inductive reactive power of the HSC, respectively. In Fig. 3, N_{TSC} increases with the capacitive reactive power which is demanded to compensate an inductive load. In this case, the major reactive power is produced by the TSCs and the residual part is produced by the inverter. However, inductive reactive power is sometimes demanded when a capacitive load is connected to the grid. The inverter only works under this condition.

B. Mathematical Model

A single-phase equivalent circuit of the HSC is shown in Fig. 4. The nonlinear load is considered as a current source, the TSCs are considered as an equivalent impedance, and the inverter is considered as a controlled current source.

In Fig. 4, the current sum of the load and TSCs I_t is detected as the input of the inverter, and G_{inv} represents the controlled gain of I_t. Thus, the output current of the inverter I_c can be expressed as:

$$I_c = G_{inv} I_t = G_{inv}(I_{TSC} + I_l) \tag{1}$$

The equivalent circuit is feasible at both the fundamental frequency and the harmonic frequencies. The subscripts 1 and h are used to indicate these two cases. When the equivalent circuit is applied at the fundamental frequency, the currents of inverter and TSCs, I_{c1} and I_{TSC1}, compensate the reactive component of the load current I_{l1q}, and the grid current I_{s1} is equal to the active component of the load current I_{l1p}, which can be expressed as:

$$\begin{cases} I_{c1} = I_{t1q} = I_{TSC1} + I_{l1q} \\ I_{s1} = I_{t1p} = I_{l1p} \end{cases} \tag{2}$$

Where I_{t1q} and I_{l1q} are the reactive components of I_{t1} and I_{c1}, respectively.

When the equivalent circuit is applied in the harmonic region, according to Kirchhoff voltage law and current law, it can be seen that:

$$\begin{cases} U_{sh} = Z_{sh} I_{sh} + Z_{TSCh} I_{TSCh} \\ I_{sh} = I_{TSCh} + I_{lh} - I_{ch} \\ U_{lh} = U_{sh} - I_{sh} Z_{sh} \end{cases} \tag{3}$$

From Equation (3), the grid harmonic current can be expressed as:

$$I_{sh} = \frac{Z_{TSCh} I_{lh}}{Z_{sh} + Z_{TSCh}} + \frac{U_{sh}}{Z_{sh} + Z_{TSCh}} - \frac{Z_{TSCh} I_{ch}}{Z_{sh} + Z_{TSCh}} \tag{4}$$

According to Equation (4), it can be seen that the grid harmonic current I_{sh} is composed of two parts, which are caused by the load harmonic current I_{lh} and the grid harmonic voltage U_{sh}, respectively. In addition, system parallel resonance occurs when $Z_{sh} + Z_{TSCh} \approx 0$. The harmonic compensating current of the inverter I_{ch} can be used to eliminate these two harmonic components.

Substituting Equation (1) into Equation (4), the grid harmonic current can be changed into:

$$I_{sh} = \frac{(1-G_{inv}) Z_{TSCh} I_{lh}}{Z_{TSCh} + (1-G_{inv}) Z_{sh}} + \frac{(1-G_{inv}) U_{sh}}{Z_{TSCh} + (1-G_{inv}) Z_{sh}} \tag{5}$$

It can be seen from Equation (5) that it is possible to totally eliminate the grid harmonic current I_{sh}, and to avoid the resonance problem between the grid and the TSCs when G_{inv} is equal to 1.

Fig. 5 shows a control block diagram of the HSC. It is equivalent to Fig. 4, and it is possible to obtain Equation (5) from Fig. 5. There is a closed loop in the control diagram, which is circled with the dotted line.

In Fig. 5, the grid voltage is viewed as the disturbance variable, and it is possible to obtain the open-loop transfer function and the closed-loop transfer function of the HSC as:

$$G_{HSC\_Open\_loop} = -G_{inv} \cdot \frac{Z_S}{Z_S + Z_{TSC}} \tag{6}$$

$$G_{HSC\_Closed\_loop} = \frac{i_s}{i_l} = \frac{(1-G_{inv}) Z_{TSC}}{Z_{TSC} + (1-G_{inv}) Z_s} \tag{7}$$

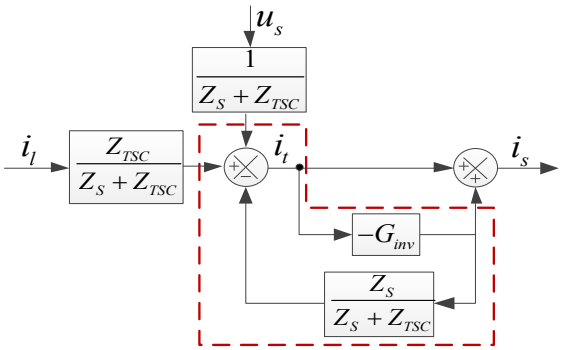

Fig. 5. Control block diagram of the HSC.

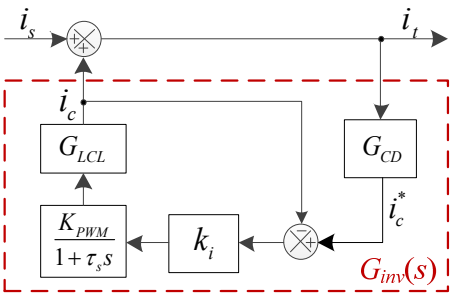

Fig. 6. Current control block diagram of the inverter.

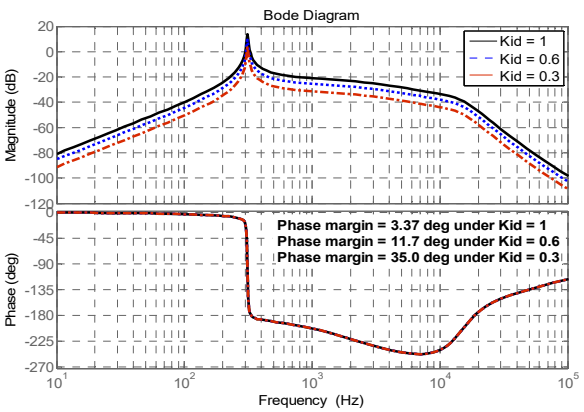

Fig. 7. Bode diagram of the HSC open-loop transfer function under different k_{id}.

III. Current Control Method

A. Mathematical Model of the Inverter

Fig. 6 shows a current control block of the inverter. G_{CD} denotes the reactive and harmonic current detection link; τ_s denotes the switching period; $K_{PWM} = U_d / U_t$, where U_d denotes the DC link voltage and U_t denotes the amplitude of the triangular carrier [17]; k_i denotes the proportionality coefficient of the current controller; and G_{LCL} denotes the LCL-type filter link.

Considering the filtering link and computational delay of the current detection link, G_{CD} can be approximately expressed as:

$$G_{CD} = \frac{i_c^*}{i_t} = \frac{k_{id}}{1+\tau_1 s} \tag{8}$$

Where k_{id} denotes the current compensation coefficient, and τ_1 denotes the delay time.

The LCL-type filter is a third-order filtering link, and its transfer function can be expressed as:

$$G_{LCL} = \frac{R_d C s + 1}{L_1 L_2 C s^3 + (L_1+L_2) R_d C s^2 + (L_1+L_2) s} \tag{9}$$

Where R_d is the damping resistor, C is the filter capacitor, L_1 is the inverter-side filter inductor, and L_2 is the grid-side filter inductor.

Thus, the transfer function of the inverter is expressed as:

$$\begin{aligned} G_{inv} &= G_{CD} \cdot \frac{i_c}{i_c^*} \\ &= \frac{k_{id} k_i K_{PWM} (R_d C s + 1)}{T_1 s^5 + T_2 s^4 + T_3 s^3 + T_4 s^2 + T_5 s + T_6} \end{aligned} \tag{10}$$

Where T_1~T_6 are respectively expressed as:

$$\begin{cases} T_1 = L_1 L_2 C \tau_s \tau_1 \\ T_2 = L_1 L_2 C(\tau_s + \tau_1) + (L_1+L_2) R_d C \tau_s \tau_1 \\ T_3 = L_1 L_2 C + (L_1+L_2)(R_d C \tau_s + R_d C T_1 + \tau_s \tau_1) \\ T_4 = (L_1+L_2)(R_d C + \tau_s) + (k_i K_{PWM} R_d C + L_1 + L_2)\tau_1 \\ T_5 = k_i K_{PWM} R_d C + L_1 + L_2 + k_i K_{PWM} \tau_1 \\ T_6 = k_i K_{PWM} \end{cases} \tag{11}$$

According to Equation (6), (10) and (11), it is possible to obtain a bode diagram of the HSC open-loop transfer function under different k_{id} as Fig. 7.

From Fig. 7, a resonant peak exists in the Bode diagram, and a -180° phase jump occurs at this resonant frequency. This causes an output current oscillation and destabilizes the HSC system. However, this resonant peak is influenced by the value of k_{id}, and a decreasing k_{id} helps damp the resonant peak and increases the system phase margin.

B. ROGI-based Selective Current Compensation Method

Based on Fig. 7, it is feasible for the HSC system to get a sufficient phase margin by decreasing k_{id}. However, high gains at the fundamental and harmonic frequencies are required to ensure a high current compensation precision. The selective current compensation method is appropriate to satisfy this under a low k_{id}, and a second order generalized integrator (SOGI) is generally adopted to obtain a high enough gain at a specific frequency and to track the ac signal with zero steady-state error. The transfer function of a SOGI is expressed as:

$$G_{SOGI}(s) = \frac{2K_I s}{s^2 + \omega_h^2} = \frac{K_I}{s - j\omega_h} + \frac{K_I}{s + j\omega_h} \tag{12}$$

Where K_I is the integral gain, and ω_h is the resonant frequency. From Equation (12), the SOGI can be viewed as a combination of two first order generalized integrators with the same resonant frequency and opposite sequences. For this reason, the first order generalized integrator is referred to as

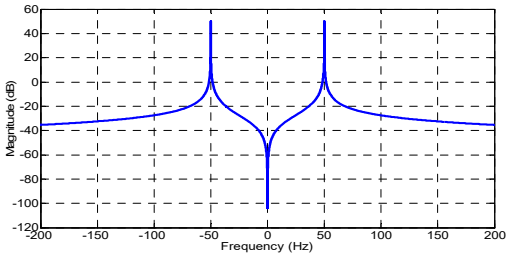

(a) Amplitude-frequency response of $2K_I s/(s^2+\omega_1^2)$.

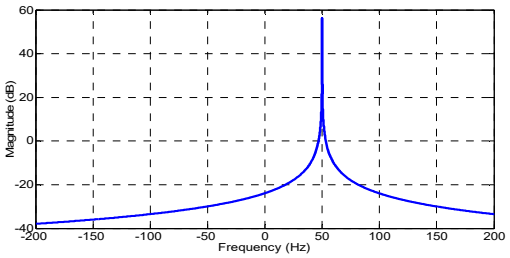

(b) Amplitude-frequency response of $2K_I/(s-j\omega_1)$.

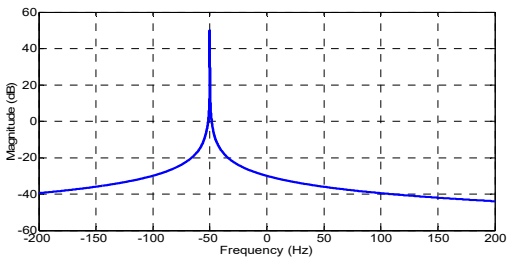

(c) Amplitude-frequency response of $2K_I/(s+j\omega_1)$.

Fig. 8. Amplitude-frequency responses of the SOGI and ROGI.

the ROGI [24].

Fig. 8 presents the amplitude-frequency responses of the SOGI and two ROGIs in Equation (12). In Fig. 8, $\omega_h=\omega_1$, and ω_1 is the fundamental frequency.

As shown in Fig. 8, the SOGI obtains an infinite gains at both the fundamental positive and negative sequences, whereas the ROGI obtains an infinite gain at only one of the two sequences. This indicates that the ROGI is characterized as sequence-decoupled frequency selection and that it can assign different gains for the positive and negative sequence components of the ac signal. Consequently, the ROGI has more control freedom degrees and better control flexibility when compared to the SOGI.

The ROGI in Equation (12) has an infinite gain at the resonant frequency, which tends to degrade the stability of the control system. Meanwhile, the grid frequency fluctuation or the resonant frequency deviation caused by the discretization process of the ROGI controller result in a sharp decline of the actual controller gain. Given the above issues, an improved ROGI is proposed by introducing a damping term, and its transfer function is expressed as:

$$G_{ROGI}(s)=\frac{K_I\cdot\omega_c}{s-j\omega_h+\omega_c} \tag{13}$$

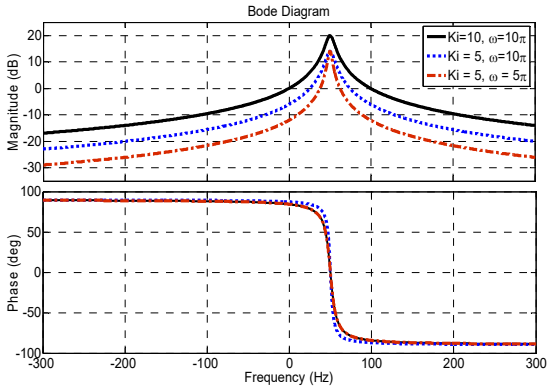

Fig. 9. Frequency response of the improved ROGI.

Where K_I is the integral gain, ω_h is the resonant frequency of the ROGI controller, and ω_c is the added damping term.

Fig. 9 presents the frequency response of the improved ROGIs with different K_I and ω_c parameters, when the ROGI resonant frequency is $\omega_h=+\omega_1=50\cdot2\pi$.

According to Fig. 9, the improved ROGI gain at the resonant frequency is independently adjusted by K_I. The bandwidth and phase characteristics at the resonance frequency are determined by the ROGI damping term ω_c. Consequently, the two issues are solved in the improved ROGI and the frequency response of the improved ROGI can be adjusted simply by changing K_I and ω_c.

A balanced three-phase system generally contains only $(6k\pm1)$th (k = 1, 2, 3...) harmonic currents because most power conversion processes involved in the industrial apparatus (e.g., diode rectifier loads) produce these harmonic components. When the grid voltage or load condition is unbalanced, each $(6k\pm1)$th harmonic contains both positive and negative sequence components. However, in most cases, the unbalanced condition of the grid voltage or load is not severe (i.e., mostly below 10%). In such cases, each harmonic mainly contains a certain sequence component which satisfies $(\pm6k+1)$ (k = 1, 2, 3...), and the improved ROGI unit in Equation (13) can be introduced to cope with the corresponding harmonic signal.

In this study, two ROGIs separately tuning at $\pm\omega_1$ are adopted for the fundamental current because the fundamental unbalance component cannot be neglected relative to the harmonics. Considering that the percentage of non-linear load harmonic current components above the 25th in the total harmonic currents is less than 2%, a series of paralleled ROGIs tuning at $(\pm6k+1)\omega_1$ (k = 1, 2, 3, 4) are selected to constitute the harmonic controller. In addition, a proportional controller with the gain K_p is also included to ensure good dynamic performance. Thus, the whole current controller of the ROGI-based selective current compensation method is expressed as:

$$G_C(s)=K_p+\frac{K_{I(-1)}\cdot\omega_{c(-1)}}{s+j\omega_1+\omega_{c(-1)}}+\sum_{n=\pm6k+1}\frac{K_{I(n)}\cdot\omega_{c(n)}}{s-jn\omega_1+\omega_{c(n)}} \tag{14}$$

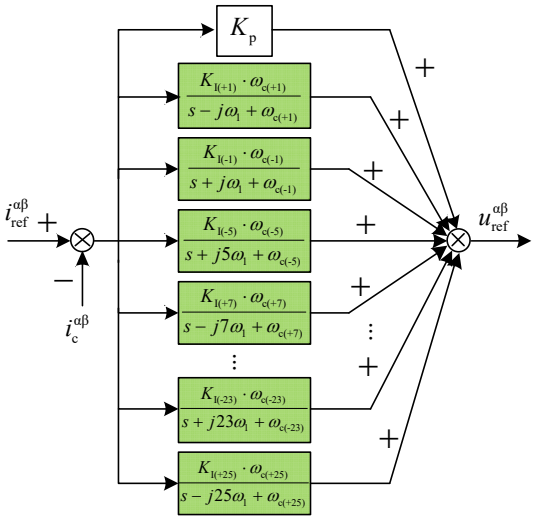

Fig. 10. Diagram of the ROGI-based current controller.

Where k = 0, 1, 2, 3, 4, and it is possible to depict a diagram of the proposed ROGI-based current controller as Fig. 10.

IV. Switch Control Strategy

In the HSC, the inverter and the TSCs should cooperate closely to implement accurate reactive power compensation for non-linear loads. However, three problems exist.

1) I_t is used in Fig. 1 to detect the load reactive power rather than the load current I_l. Thus, it is necessary to precisely recognize which causes the detected reactive power to change between the load change and the TSC switching. Otherwise, the wrong recognition may result in repeated switching of the TSCs.

2) It matters in terms of how to control the TSCs in time when the load reactive current fluctuates sharply, which may also cause the TSCs to lose control.

3) The switch time of the TSCs and the resulting current fluctuation should be taken into account because the TSCs and the inverter have different dynamic response speeds.

To solve the above issues, a switch control strategy is proposed as follows.

Step 1: Extract the fundamental reactive component of I_t.

Firstly, it is necessary to transform I_t from the *abc* stationary frame to the *dq* rotating frame, and obtain its *d*-axis component I_{td} and *q*-axis component I_{tq}. Then, two DC components $\overline{I_{td}}$ and $\overline{I_{tq}}$ can be extracted by filtering I_{td} and I_{tq} with low-pass filters (LPF), and they satisfy Equation (15):

$$\begin{bmatrix}\overline{I_{td}}\\ \overline{I_{tq}}\end{bmatrix}=\begin{bmatrix}\sqrt{3}I_{t1}\cos\theta_1\\ -\sqrt{3}I_{t1}\sin\theta_1\end{bmatrix} \tag{15}$$

Where I_{t1} is the fundamental component of I_t, and θ_1 is the phase difference between grid voltage U_s and I_{t1}.

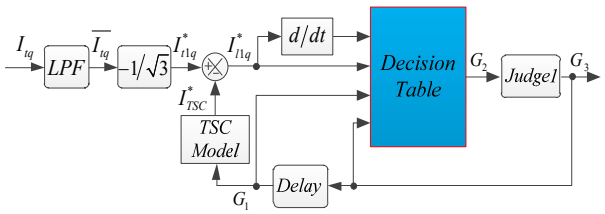

Fig. 11. Switch control diagram of the HSC.

I_{t1q} denotes the reactive current component of I_{t1}, and it is equal to $I_{t1}sin\theta_1$. Thus, I_{t1q} can be expressed as:

$$I_{t1q}=I_{t1}\sin\theta_1=-\frac{\overline{I_{tq}}}{\sqrt{3}} \tag{16}$$

In this way, it is possible to deduce the fundamental reactive current component I_{t1q} from I_t.

Step 2: Decide the switch table of the TSCs.

Fig. 11 depicts a switch control diagram of the HSC. In Fig. 11, I_{t1q}^* is the deduced fundamental reactive component from I_t, I_{TSC}^* is the calculated TSC current, and I_{l1q}^* is the fundamental reactive component of I_l. G is the switch table of the TSCs, in which 0 denotes switching off and 1 denotes switching on. Specially, G_1 is the switch table in the present period. G_2 is the possible switch table in the next period. G_3 is the switch table which meets *Judge*1 and will be implemented in the next period.

From Fig. 11, the proposed switch control strategy is used to predict the possible switch table in the next period G_2, and to confirm whether G_2 will be implemented in the next period. Generally, the fundamental reactive current component I_{t1q}^* is deduced from I_t. I_{TSC}^* is calculated according to the TSC model and the present switch table G_1 because the TSC current is not directly detected in the HSC. Thus, I_{l1q}^* will be obtained by subtracting I_{TSC}^* from I_{t1q}^*. Four input signals: I_{l1q}^*, dI_{l1q}^*/dt, G_1, and G_3 are sent to the decision table, and G_2 is subsequently deduced. In order to avoid repeatedly switching the TSCs, *Judge*1 is employed to decide whether G_2 will be implemented in the next period. If G_2 meets *Judge*1, G_2 is assigned to G_3 and will be operated; if G_2 does not meet *Judge*1, G_1 is assigned to G_3 and the switch table of the TSCs does not change. In addition, a *Delay* link is added between G_2 and G_1 because the response time of the TSCs cannot be neglected.

A program flow diagram of the switch control strategy is shown in Fig. 12. *Judge*1 and *Delay* are both identified with the dotted line. In *Judge*1, $\left|dI_{l1q}^*/dt\right|<\Delta$ needs to be met ten times in a row to ensure that the switching of the TSCs can be operated only when the load reactive power remains steady. In the *Delay*, Z counts up to 100 from 0 so that the transient process of switching the TSCs totally ends and the HSC is restored to the steady state.

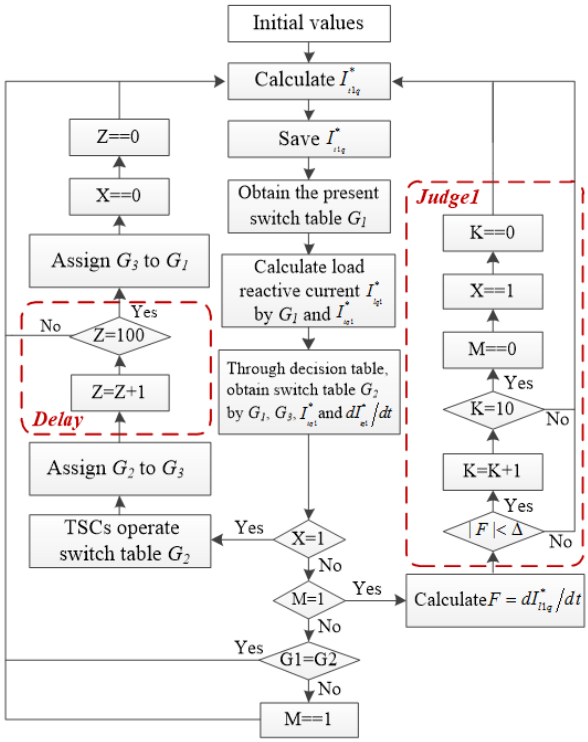

Fig. 12. Program flow diagram of the switch control strategy.

TABLE I
DECISION TABLE FOR TWO TSCS

dI^*_{l1q}/dt	Switch table G3	Switch table G1	I^*_{l1q}	Switch table G2
$\lvert dI^*_{l1q}/dt\rvert<\Delta$	$G_1=G_3$	(0,0)	$I^*_{l1q}<0$	(0,0)
		(0,1)	$I^*_{l1q}<-I_1$	(0,0)
			$-I_1<I^*_{l1q}<0$	(0,1)
		(1,0)	$I^*_{l1q}<-I_2$	(0,0)
			$-I_2\le I^*_{l1q}<-I_1$	(0,1)
			$-I_1<I^*_{l1q}<0$	(1,0)
		(1,1)	$I^*_{l1q}<-I_3$	(0,0)
			$-I_3\le I^*_{l1q}<-I_2$	(1,0)
			$-I_2\le I^*_{l1q}<-I_1$	(0,1)
			$-I_1<I^*_{l1q}<0$	(1,1)
		Random	$0<I^*_{l1q}<I_1$	(0,0)
			$I_1\le I^*_{l1q}<I_2$	(0,1)
			$I_2\le I^*_{l1q}<I_3$	(1,0)
			$I_3\le I^*_{l1q}$	(1,1)
	$G_1\neq G_3$	Random	Random	Unchanged

In the HSC prototype, two TSCs are supplied and the decision table is shown as Table I. In Table I, I_1 denotes the current of the first TSC, I_2 denotes the current of the second TSC, and I_3 denotes the current sum of the two TSCs.

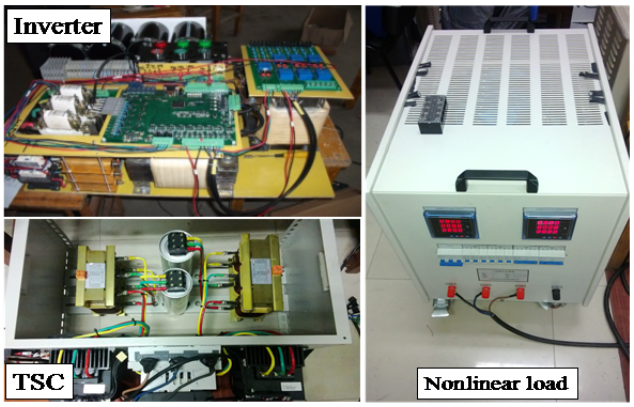

Fig. 13. Three-phase three-wire HSC experimental prototype.

TABLE II
PARAMETERS OF THE HSC EXPERIMENTAL PROTOTYPE

Parameter	Value
Grid voltage U_s	380 V
DC side voltage of inverter U_{dc}	780 V
Inverter-side inductor L_1	100 μH
Grid-side inductor L_2	50 μH
Filter capacitor C_f	30 μF
Damping resistor R_d	0.1Ω
Diode rectifier resistive load R_{load}	5.8Ω
Diode rectifier inductive load L_{load}	1 mH
Inductor of the 1st TSC L_{f1}	5.133 mH
Capacitor of the 1st TSC C_{f1}	46.1 μF
Inductor of the 2nd TSC L_{f2}	3.423 mH
Capacitor of the 2nd TSC C_{f2}	69.1 μF

V. EXPERIMENTAL RESULTS AND ANALYSIS

Experiments are implemented on a 20KVA three-phase three-wire HSC prototype, which is depicted in Fig. 1. A photo of the prototype is shown in Fig. 13.

The load consists of two parts: a three-phase diode rectifier with RL loads and a three-phase inductive load. They are connected in parallel to produce harmonics and reactive current. The key parameters of the prototype are listed in Table II. The control platform is implemented on a TMS320F28335 DSP control board. Both the sampling and switching frequencies are set to 15 kHz. A Yokogawa DL850 is used as the measurement instrument.

A. Steady-state Performance Comparison of Different Current Control Methods

Fig. 14(a) shows a waveform of the grid current with a nonlinear load and a 7Kvar inductive load before the HSC is used. Fig. 14(b) shows the frequency spectrum of the grid current. The total harmonic distortion (THD) of the grid current is 21.8%. Fig.14(c) shows information about the reactive power and power factor (PF). The total 9.48Kvar reactive power is produced and injected into the grid under this load condition, and the PF of the PCC is 0.85.

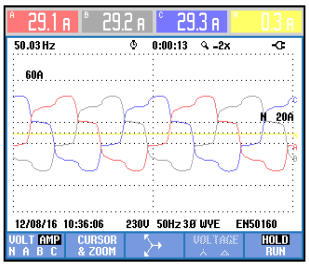

(a) Phase currents.

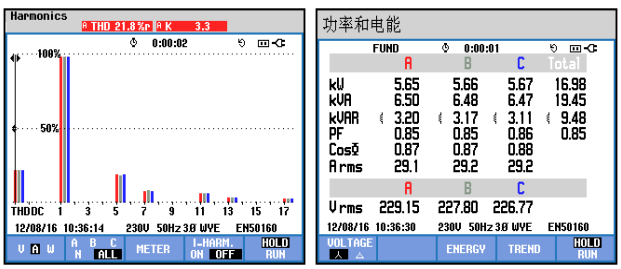

(b) Frequency spectrum. (c) Power factor.

Fig. 14. Waveform of the grid current without the HSC.

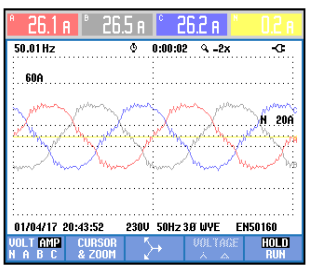

(a) Phase currents.

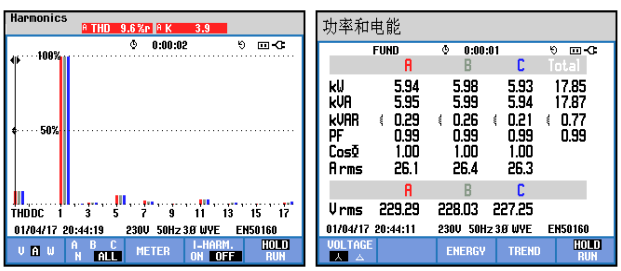

(b) Frequency spectrum. (c) Power factor.

Fig. 15. Steady-state performance with a traditional PI controller.

Fig. 15 shows experimental results of the steady-state grid current when the HSC with a traditional PI controller is used. The 1st TSC has been switched into the grid. As shown in Fig. 15(b), the THD of the grid current is reduced from 26.1% to 9.6%. As shown in Fig. 15(c), the PF of the PCC is improved from 0.85 to 0.99.

Fig. 16 shows experimental results of the steady-state grid current when the HSC with the ROGI-based current controller is used. The 1st TSC has been switched into the grid. As shown in Fig. 16, the grid current is almost sinusoidal with a low THD of 3.3%, and the PF of the PCC reaches nearly 1.00.

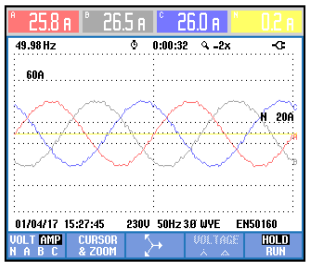

(a) Phase currents.

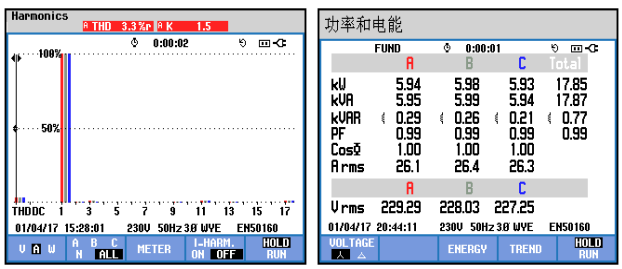

(b) Frequency spectrum. (c) Power factor.

Fig. 16. Steady-state performance with the ROGI-based current controller.

From Fig. 14 - 16, the THD of the grid current and the PF of the PCC have both been improved when the HSC is operated, which confirms that this device has a good steady performance for harmonic suppression and reactive power compensation. Furthermore, the proposed ROGI-based controller can realize a lower THD and a higher PF than a traditional PI controller. This result shows that the proposed ROGI-based controller has a better steady current control capability.

B. Dynamic Response Comparison of Different Switch Control Strategies

Fig. 17 - 19 illustrate experimental results of the dynamic response when the conventional switch control strategy [22] and the proposed switch control strategy are adopted. During the experimental process, the load changes in the following order: no load, nonlinear load, nonlinear load + 7Kvar inductive load, nonlinear load + 10Kvar inductive load, nonlinear load + 7Kvar inductive load, nonlinear load, no load. In each figure, from top to bottom, G_{TSC1} and G_{TSC2} are the switch control signals of the two TSCs in which the high level denotes switching off and the low level denotes switching on, U_a is the a-phase voltage of the PCC, I_{la} is the a-phase load current, I_{sa} is the a-phase grid current, I_{ca} is the a-phase current of the inverter, and I_{TSCa} is the a-phase current of the TSC.

Fig. 17 shows experimental results of the dynamic response when a conventional switch control strategy with a fixed time delay of 0.14s is used. Waveforms during the entire experimental process are illustrated in Fig. 17(a). As shown, the 1st TSC is switched on when the 7Kvar inductive load is added; the 1st TSC is switched off while the 2nd TSC

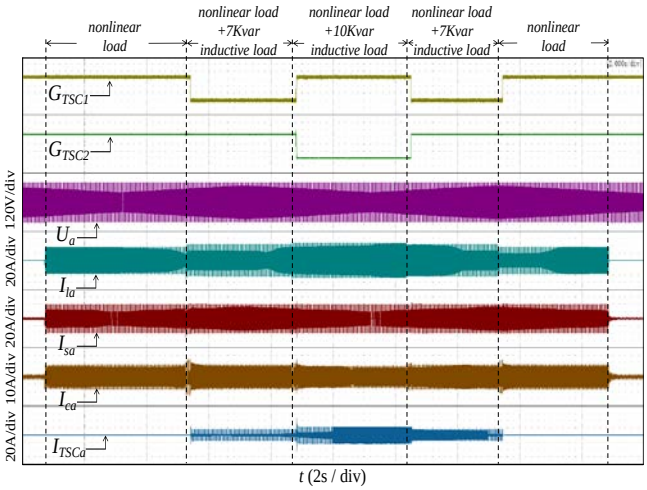

(a) Waveforms during the whole experimental process.

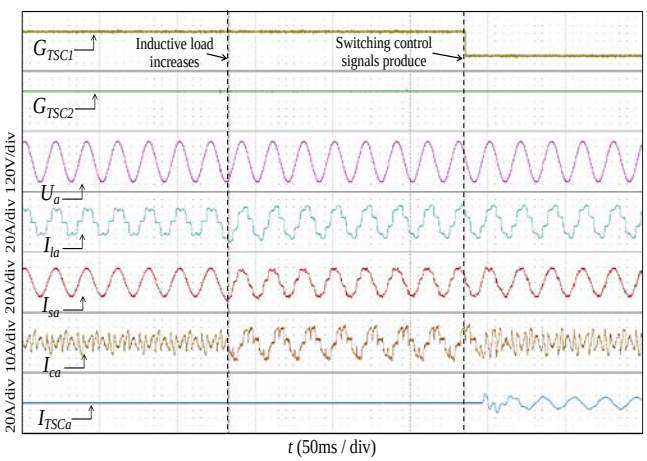

(b) Waveforms when a 7Kvar inductive load is added.

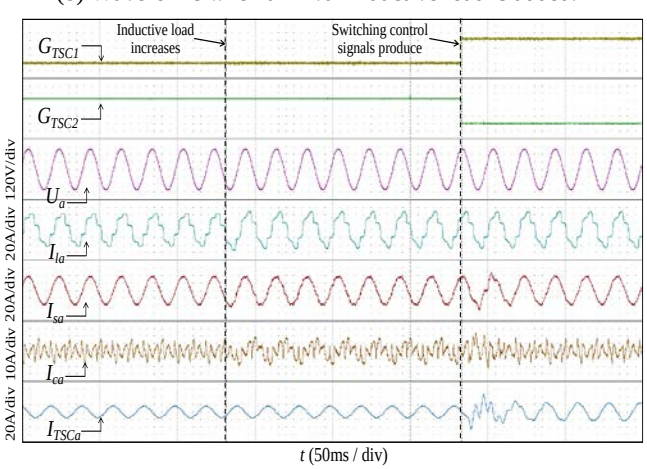

(c) Waveforms when the inductive load increases to 10Kvar.

Fig. 17. Dynamic response when a conventional switch control strategy with a fixed time delay of 0.14s is used.

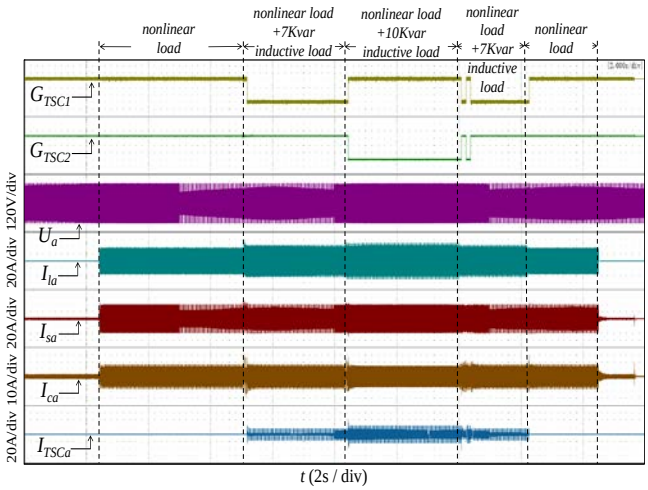

(a) Waveforms during the whole experimental process.

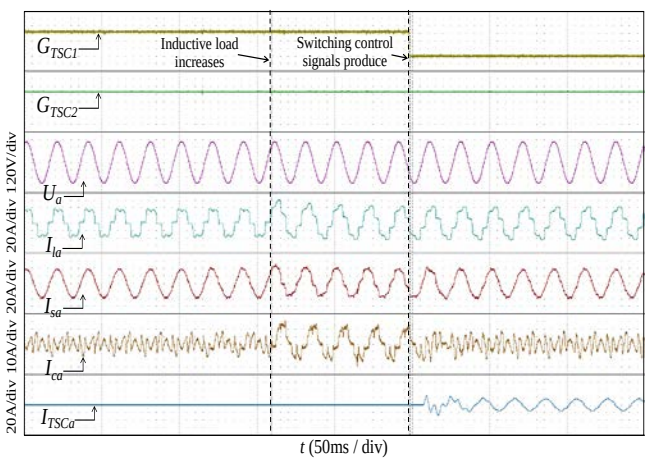

(b) Waveforms when a 7Kvar inductive load is added.

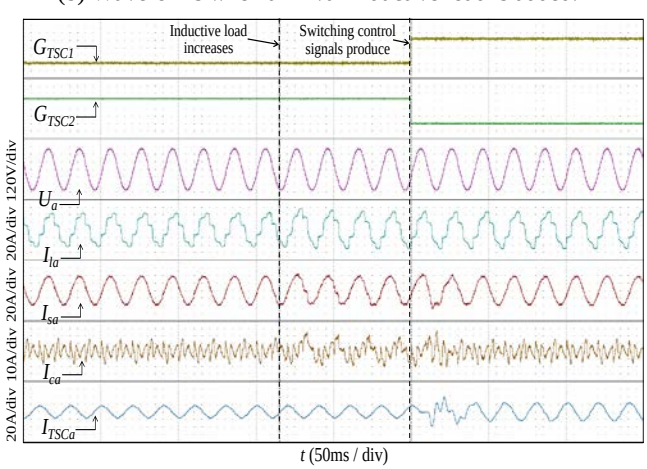

(c) Waveforms when the inductive load increases to 10Kvar.

Fig. 18. Dynamic response when a conventional switch control strategy with a fixed time delay of 0.08s is used.

is switched on when the inductive load increases to 10Kvar from 7Kvar; and right switch control signals are also produced when the inductive load decreases. This result confirms that the switch control strategy in Fig. 17 can precisely recognize changes in the load reactive power and correctly implement the switching of the TSCs. Fig. 17(b) shows waveforms when a 7Kvar inductive load is added. As shown, the measured time interval between increasing the inductive load and generating the switching control signals is approximately 0.1562s. Fig. 17(c) shows waveforms when

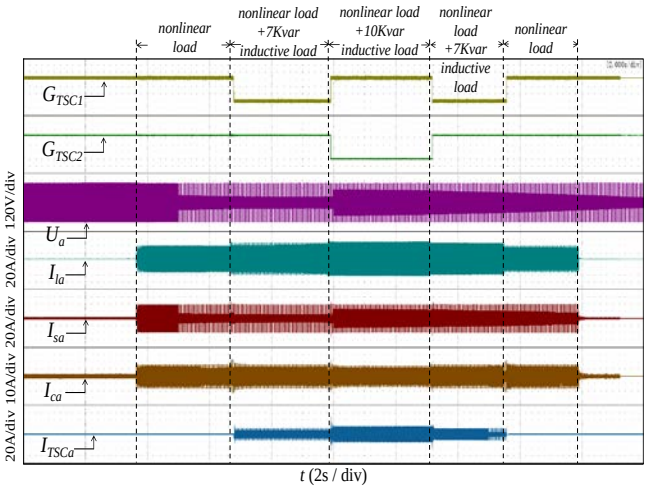

(a) Waveforms during the whole experimental process.

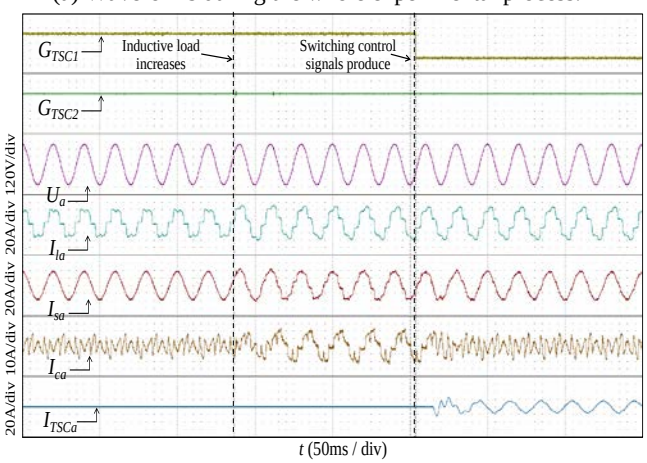

(b) Waveforms when the a 7Kvar inductive load is added.

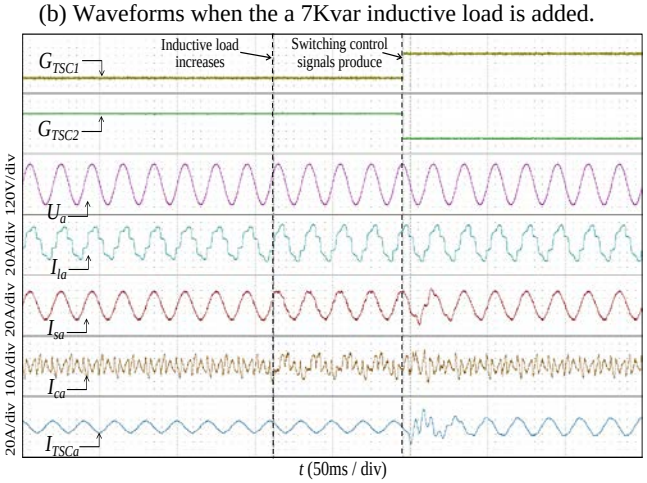

(c) Waveforms when the inductive load increases to 10Kvar.

Fig. 19. Dynamic response when the proposed switch control strategy is used.

the inductive load increases to 10Kvar from 7Kvar, and the measured time interval in Fig. 17(c) is nearly 0.1494s. The two time intervals are almost the same, and the difference between them may be caused by different relay circuits. In addition, they are both very close to the fixed time delay of 0.14s.

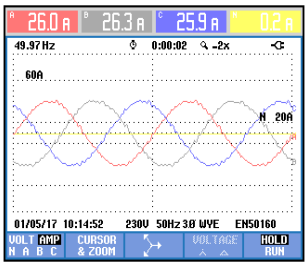

(a) Phase currents.

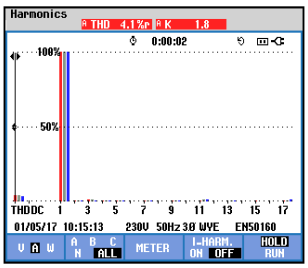

(b) Frequency spectrum.

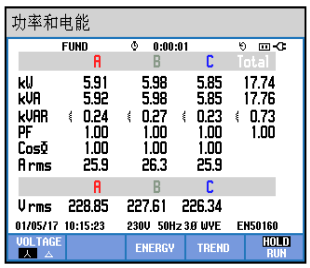

(c) Power factor.

Fig. 20. Steady-state performance when a topology for detecting the load current I_l is adopted.

Fig. 18 shows the dynamic response when a conventional switch control strategy with a fixed time delay of 0.08s is adopted. As shown in Fig. 18(a), a malfunction of the TSCs occurs because reducing the time delay may cause the switching of TSCs to be operated during the oscillation process of the load reactive power. Moreover, the time interval in Fig. 18(b) is measured to be 0.0897s, and the time interval in Fig. 18(c) is 0.0847s. The two measured time intervals are nearly the same and very close to the fixed time delay of 0.08s.

Fig. 19 shows the dynamic response of the proposed switch control strategy. As shown in Fig. 19(a), the switching of the TSCs is implemented precisely when the load condition changes. In addition, the time interval in Fig. 19(b) is measured to be 0.1167s, while the time interval in Fig. 19(c) is 0.0837s. The former time interval is obviously longer than the latter one because it takes the grid current Isa a longer time to restore to the steady state when a 7Kvar inductive load is added than when a 3Kvar inductive load is added. This result demonstrates that the proposed switching strategy has no fixed time delay, and that the time interval between recognizing the change of the load reactive power and producing the switch signals is adjusted depending on the practical load conditions.

From Fig. 17-19, it can be seen that the conventional switch strategy needs a long enough time delay against the malfunction of the TSCs. However, the time delay is difficult to set because the practical load condition is usually uncertain. In comparison with the conventional method, the proposed switch control strategy can implement a precise and fast switching of the TSCs without changing the time delay under different load changes. Thus, it is more suitable for practical

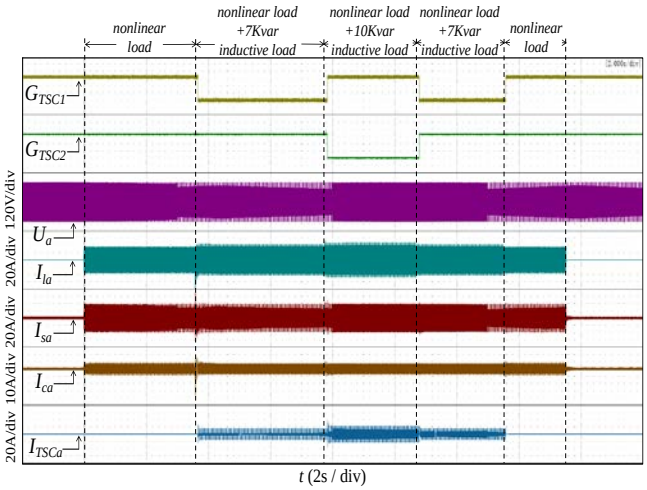

(a) Waveforms during the whole experimental process.

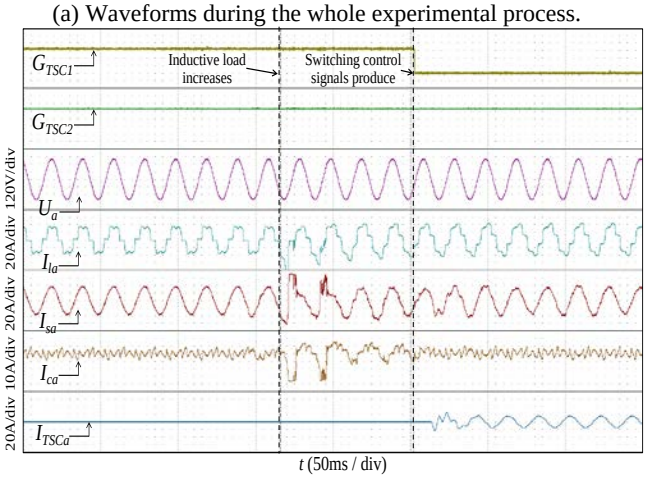

(b) Waveforms when a 7Kvar inductive load is added.

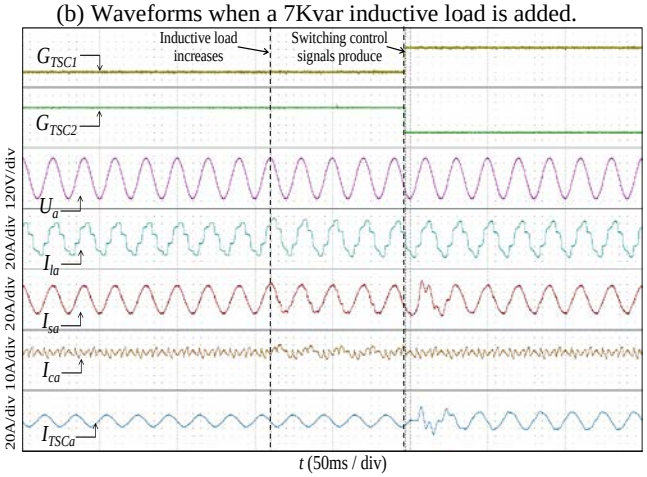

(c) Waveforms when the inductive load increases to 10Kvar.

Fig. 21. Dynamic response when a conventional switch control strategy with a fixed time delay of 0.08s is adopted in the topology for detecting the load current I_l.

systems.

C. Performance Comparison between Different Topologies

Fig. 20-21 represent experimental results of the steady-state grid current and experimental results of the dynamic response when the load current I_l is detected instead of the current sum of the load and the TSCs I_t. In this topology, the ROGI-based current controller and the conventional switch control strategy are adopted.

Fig. 20 shows experimental results of the steady-state grid current under the same load condition as Fig. 16. The 1st TSC has been switched into the grid. As shown in Fig. 20(b) and (c), the grid current is almost sinusoidal with a THD of 4.1%, and the PF of the PCC reaches 1.00. In Fig. 16, it can be seen that the steady-state grid current has a lower THD of 3.3%. Comparing Fig. 20 and 16, the topology for detecting the load current I_l cannot achieve an equally good harmonic suppression effect as that for detecting I_t. This is because the harmonics caused by the TSCs are allowed into the grid when the topology for detecting I_l is used.

Fig. 21(a) illustrates waveforms of the dynamic response when a conventional switch control strategy with a fixed time delay of 0.08s is adopted in the topology for detecting the load current I_l. As shown in Fig. 21(b) and 21(c), the two time intervals are 0.0862s and 0.0859s, respectively, which are both close to 0.08s. Compared with Fig. 18(a), there is no malfunction of the TSCs under the same time delay. This is because the switching of the TSCs has no influences on recognizing the load reactive power.

From Fig. 20-21, in the topology for detecting the load current I_l, the change of the load reactive power is directly recognized. Thus, the switching of the TSCs can be correctly implemented in spite of a short time delay. However, the harmonics caused by the TSCs are allowed into the grid, which leads to a poor steady harmonic suppression effect. In addition, considering that the current of the TSCs is not detected, a TSC model is needed so that the inverter can precisely compensate the residual reactive power when the TSC is switched on.

In conclusion, Table III is given to summarize the above experimental results.

VI. CONCLUSIONS

This paper proposed a HSC system that is composed of a small-capacity inverter and multigroup TSCs. The proposed HSC combined the advantages of both inverters in terms of their precise and fast current compensation and TSCs in terms of their large-capacity reactive power compensation at a low cost. The structure and mathematical models of the HSC are both given. Then the control method is presented. For the inverter, a ROGI-based current control method is used to achieve high-performance current compensation. For the TSCs, a switch control strategy is proposed to implement precise and fast switching of the TSCs. When compared with the conventional switch strategy, the proposed strategy is more suitable for practical systems because it does not need to change the time delay under different load changes. A 20KVA prototype was developed in the laboratory.

TABLE III
PARAMETERS OF THE SHUNT APF PROTOTYPE

	PI current controller	Proposed ROGI-based current controller	Conventional switch control strategy	Proposed switch control strategy	Topology for detecting the load current I_l	Adopted Topology for detecting the current sum of the load and the TSCs I_t
Steady-state current compensation precision	THD=9.6% PF=0.99	THD=3.3% PF=1.00			THD=4.1% PF=1.00	THD=3.3% PF=1.00
Whether to implement the correct switching of the TSCs			Yes (with a proper time delay)	Yes		
Whether a fixed time delay is needed			Yes	No		
How to recognize a change of the load reactive power					Directly	Indirectly

Experimental result comparisons between different control methods and topologies validated the theoretical analysis.

ACKNOWLEDGMENT

This work was supported in part by the National Key Basic Research Program of China (Project no. 973) under Grant no. 2013CB035604.

REFERENCES

[1] H. Akagi, "Active harmonic filters," in *Proceeding of the IEEE*, Vol. 93, No. 12, pp. 2128-2141, Dec. 2005.

[2] F. Blaabjerg, R. Teodorescu, M. Liserre, and A. V. Timbus, "Overview of control and grid synchronization for distributed power generation systems," *IEEE Trans. Ind. Electron*., Vol. 53, No. 5, pp. 1398-1409, Oct. 2006.

[3] Z. Zeng, H. Yang, S. Tang, and R. Zhao, "Objective-oriented power quality compensation of multi-functional grid-tied inverters and its application in micro-grids," *IEEE Trans. Power Electron*., Vol. 30, No. 3, pp. 1255-1265, Mar. 2015.

[4] N. Zhu, S. Vadari, and D. Hwang, "Analysis of a static VAR compensator using the dispatcher training simulator," *IEEE Trans. Power Syst*., Vol. 10, No. 3, pp. 1234-1242, Aug. 1995.

[5] D. T. Rizy, E. W. Gunther, and M. F. McGranaghan, "Transient and harmonic voltages associated with automated capacitor switching on distribution systems," *IEEE Trans. Power Syst.*, Vol. PER-7, No. 8, pp. 49-50, Aug. 1987.

[6] E. N. Lerch, D. Povh, and L. Xu, "Advanced SVC control for damping power system oscillations," *IEEE Trans. Power Syst*., Vol. 6, No. 2, pp. 524-535, May 1991.

[7] J. Zhang, J. Y. Wen, S. J. Cheng, and J. Ma, "A novel SVC allocation method for power system voltage stability enhancement by normal forms of diffeomorphism," *IEEE Trans. Power Syst*., Vol. 22, No. 4, pp. 1819-1825, Nov. 2007.

[8] M. Wien, H. Schwarz, and T. Oelbaum, "Performance analysis of SVC," *IEEE Trans. Circuits Syst. Video Technol*., Vol. 17, No. 9, pp. 1194-1203, Sep. 2007.

[9] R. Guzman, L. G. de Vicuna, J. Morales, and M. Castilla, "Model-based control for a three-phase shunt active power filter," *IEEE Trans. Ind. Electron*., Vol. 63, No.7, pp. 3998-4007, Jul. 2016.

[10] M. M. Hashempour, M. Savaghebi, J. C. Vasquez, and J. M. Guerrero, "A control architecture to coordinate distributed generators and active power filters coexisting in a microgrid." *IEEE Trans. Smart Grid*., Vol. 7, No. 5, pp. 2325-2336, Sep. 2016.

[11] Y. Tang, P. C. Loh, P. Wang, F. H. Choo, F. Gao, and F. Blaabjerg, "Generalized design of high performance shunt active power filter with output LCL filter," *IEEE Trans. Ind. Electron*., Vol. 59, No. 3, pp. 1443-1452, Mar. 2012.

[12] A. Luo, Z. Shuai, W. Zhu, R. Fan, and C. Tu, "Development of hybrid active power filter based on the adaptive fuzzy dividing frequency-control method," *IEEE Trans. Power Del.*, Vol. 24, No. 1, pp. 424-432, Jan. 2009.

[13] C. Lam, W. Choi, M. Wong, and Y. Han, "Adaptive dc-link voltage-controlled hybrid active power filters for reactive power compensation," *IEEE Trans. Power Electron*., Vol. 27, No. 4, pp. 1758-1772, Apr. 2012.

[14] A. Bhattacharya, C. Chakraborty, and S. Bhattacharya, "Parallel connected shunt hybrid active power filters operating at different switching frequencies for improved performance," *IEEE Trans. Ind. Electron*., Vol. 59, No. 11, pp. 4007-4019, Nov. 2012.

[15] A. Luo, S. Peng, C. Wu, J. Wu, and Z. Shuai, "Power electronic hybrid system for load balancing compensation and frequency-selective harmonic suppression," *IEEE Trans. Ind. Electron.*, Vol. 59, No. 2, pp. 723-732, Feb. 2012.

[16] Z. Shuai, A. Luo, Z. J. Shen, W. Zhu, Z. Lv, and C. Wu, "A dynamic hybrid var compensator and a two-level collaborative optimization compensation method," *IEEE Trans. Power Electron*., Vol. 24, No. 9, pp. 2091-2100, Sep. 2009.

[17] A. Luo, Z. Shuai, W. Zhu, and Z. J. Shen, "Combined system for harmonic suppression and reactive power compensation," *IEEE Trans. Ind. Electron*., Vol. 56, No. 2, pp. 418-428, Feb. 2009.

[18] M. I. M. Montero, E. R. Cadaval, and F. B. Gonzalez, "Comparison of control strategies for shunt active power filters in three-phase four-wire systems," *IEEE Trans. Power Electron.*, Vol. 22, No. 1, pp. 229-236, Jan. 2007.

[19] A. Luo, Z. Shuai, W. Zhu, R. Fan, and C. Tu, "Development of hybrid active power filter based on the adaptive fuzzy dividing frequency-control method," *IEEE Trans. Power Del*., vol. 24, no. 1, pp. 424-432, Jan. 2009.
[20] J. Matas, L. G. de Vicuna, J. M. Guerrero, and M. Castilla, "Feedback linearization of a single-phase active power filter via sliding mode control," *IEEE Trans. Power Electron*., Vol. 23, No. 1, pp. 116-125, Jan. 2008.
[21] B. Singh, and J. Solanki, "An implementation of an adaptive control algorithm for a three-phase shunt active filter," *IEEE Trans. Ind. Electron.*, Vol. 56, No.8, pp. 2811-2820, Aug. 2009.
[22] S. Yao, A. Luo, R. Fan, and J. Tang, "Software & hardware design of intelligent Var compensation system for low-voltage distribution system," *Electr. Power Autom. Equipment*, Vol. 24, No. 12, pp. 90 – 92, Dec. 2006.
[23] H. Chiang, J. Wang, J. Tong, and G. Darling, "Optimal capacitor placement, replacement and control in large-scale unbalanced distribution systems: Modeling and a new formulation," *IEEE Trans. Power Syst.*, Vol. 10, No. 1, pp. 356 – 362, Feb. 1995.
[24] C. A. Busada, S. G. Jorge, A. E. Leon, and J. A. Solsona, "Current Controller Based on Reduced Order Generalized Integrators for Distributed Generation Systems," *IEEE Trans. Ind. Electron*., Vol. 59, No. 7, pp. 2898-2909, Jul. 2012.

Jia-Qiang Yang was born in Jiangsu, China, in 1970. He received his Ph.D. degree in Electrical Engineering from Zhejiang University, Hangzhou, China, in 2004. He has been an Associate Professor in the College of Electrical Engineering, Zhejiang University, since 2006. He was a Research Fellow at the National University of Singapore, Singapore, from March 2011 to April 2012. His current research interests include power electronics, electric machine drives, and control strategies.

Lei Yang was born in Henan, China, in 1993. He received his B.S. degree from Zhejiang University, Hangzhou, China, in 2015, where he is presently working towards his Ph.D. degree in Electrical Engineering. His current research interests include power quality, control technology, power electronics, electric drives, and renewable energy generation.

Zi-Peng Su was born in Jilin, China, in 1993. He received his B.S. degree from Zhejiang University, Hangzhou, China, in 2015, where he is presently working towards his M.S. degree in Electrical Engineering. His current research interests include power quality, control technology, power electronics, electric drives, and renewable energy generation.